npj | clean water

Article

Published in partnership with King Fahd University of Petroleum & Minerals

https://doi.org/10.1038/s41545-024-00379-6

Magnetic core supported ethyl acetate microdrops for organic contaminants removal from water

Jia Lyu, Fengming Zhang, Ran Li, Jinlin Song, Qing Liu, Jinyu Liu & Hua Dong

Organic contaminants have increasingly become a main threat to the water environment, necessitating novel methods for removing from polluted water. In this study, a kind of magnetic ethyl acetate microdrops (Fe_3O_4@KCC-1@EA) is fabricated for this purpose The KCC-1 shell of Fe_3O_4@KCC-1 nanospheres is a layer of silica with a dendritic fibrous structure. The ethyl acetate shell of the Fe_3O_4@KCC-1@EA microdrops provides them with the properties of an organic solvent. While the magnetic core makes them magnetically manipulable. Adding Fe_3O_4@KCC-1@EA microdrops to bisphenol A-polluted water allows the contaminants to be extracted into the ethyl acetate shell. These microdrops, saturated with bisphenol A, are then easily separated from the water phase with an external magnetic field, achieving a removal rate of over 98%. Besides bisphenol A, the Fe_3O_4@KCC-1@EA microdrops could also be employed to remove other organic contaminants. This method could provide a new pathway for water purification from organic contaminants.

With the continuous growth of population and economy, more and more organic contaminants from industrial production, agricultural production, and daily life are discharged into water system. This is gradually becoming a serious threat to ecologic environment and human health[1–3]. Currently, adsorption[4–8], advanced oxidation[9–14], and filtration[15–17] are the most intensively studied methods for removal of organic contaminants from the polluted water[18–20]. During adsorption, organic contaminants are adsorbed onto the surface of adsorbents through physical and/or chemical interactions (including van der Waals forces, electrostatic interactions, hydrogen bonds, and chemical bonds)[21–23], for example, the removal of bisphenol A and ibuprofen with amyloid fibrils aerogel[24], the removal of phytochrome and acidic blue with biochar[25,26], and the removal of sulfachloropyridazine with UiO-66 metal organic framework[27]. Adsorption has advantages in low cost, easy operation, etc. However, it is usually selective, i.e., effective for some contaminants but not for the others[21]. Conversely, advanced oxidation is nonselective. It is effective for most organic contaminants[18]. The advanced oxidation of organic contaminants includes Fenton and Fenton-like reactions[28,29], photocatalysis[9,30,31], ozonation[32,33], etc. In these processes, highly active reactants, including radicals (·OH, $\cdot O_2^-$, $HO_2\cdot$), oxidants (H_2O_2, O_2, O_3), electron (e^-) and positive holes (h^+), are produced to degrade organic contaminants into smaller molecules[28,29,34], for example, the degradation of bisphenol A catalyzed by p-$CoSi_1N_3$@D[35], by KCC-1-loaded TiO_2[36], and by Co-X/KCC-1[37], the degradation of tiamulin catalyzed by Ti doped Mn_3O_4/Fe_3O_4[28], the photodegradation of perfluorooctanoic acid catalyzed by $Bi_3O(OH)(PO_4)_2$[38]. However, this method usually had disadvantages such as energy and chemical consumption, increased processing time, and higher processing cost. Moreover, as many of the degradation products form the advanced oxidation of organic contaminants are still organic contaminants, it could induce secondary pollutions. Filtration with membranes is an effective way for continuous separation of fluids[39,40]. For organic contaminants removal from water, membranes based on graphene oxide, MOFs, MXene, etc. have been widely investigated[41,42], for example, the elimination of methylene blue and direct red 81 from water with ultrathin graphene nanofiltration membranes[43], the elimination of direct red 16 and humic acid with CTS/GO-ZIF-7-coated PES membranes[44], and the elimination of antibiotic and dye contaminants with GO/ZrT-1-NH_2 framework membranes[45]. With tunable pore size, thickness and surface characteristics, the performance of these filtration membranes could be tuned to realize fast water flux and/or high separation efficiency. Membrane filtration is an efficient method for fast and continuous organic contaminant removal. While the main bottleneck at present is the high cost of membrane preparation and the pollution of membrane during use which could make the membrane blocked or lose separation efficacy[22].

Besides the above-mentioned methods, organic contaminants elimination from water could also be realized by extraction with preferred organic solvents. However, the separation of organic phase from water phase could be a key point in this process. To overcome this challenge, in the present work, we developed a kind of magnetic organic microdrops (Fe_3O_4@KCC-1@EA) for extracting organic contaminants from water (Fig. 1). The magnetic organic microdrops were fabricated by loading

College of Materials and Chemistry & Chemical Engineering, Chengdu University of Technology, Chengdu, 610059, China. e-mail: donghua@cdut.edu.cn

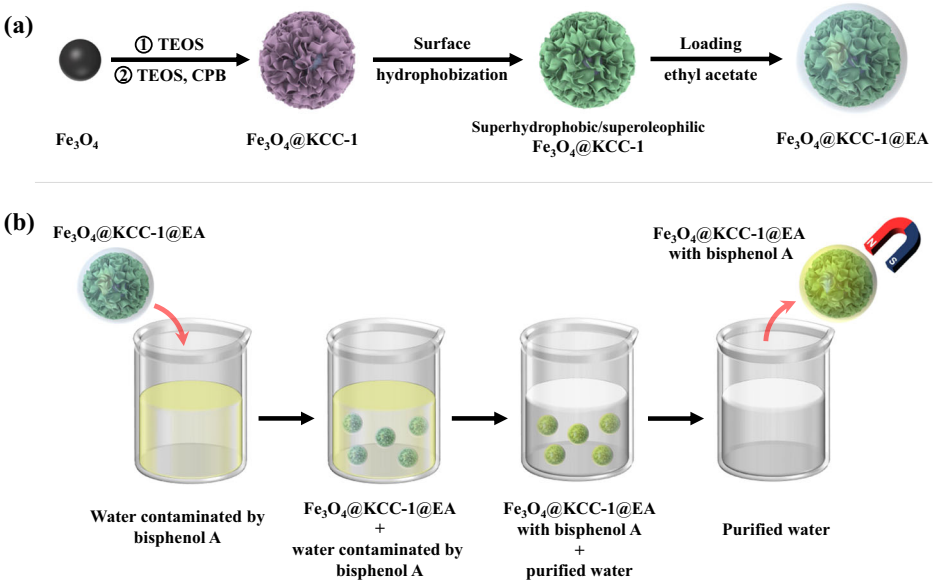

Fig. 1 | The fabrication of Fe_3O_4@KCC-1@EA microdrops and its application in BPA removal from water. a The fabrication of Fe_3O_4@KCC-1@EA microdrops; **b** The extraction of BPA from water with Fe_3O_4@KCC-1@EA microdrops.

organic solvents on the surface of superhydrophobic/superoleophilic Fe_3O_4@KCC-1 nanospheres with a magnetic core. The carrier of the microdrops, Fe_3O_4@KCC-1 nanospheres, was composed of a magnetic Fe_3O_4 core and a KCC-1 shell. The KCC-1 shell is a new kind of mesoporous silica with a dendritic fibrous structure, high surface area, large pore size and high mechanical stability[46]. As compared to conventional mesoporous silica, the high surface area of KCC-1 is not due to internal pores but owing to the radial fibers with increased accessibility. It allows the loading of active components without significant blockage of pores, which enhances the accessibility of reactants to active sites[37]. At present, KCC-1 has been applied in different processes, for example, the degradation of various refractory pollutants by the Fenton catalyst composed of DCAS Ns[47], the degradation of antibiotic and tetracycline by g-C_3N_4/KCC-1[48,49], the iron-doped fiber-structured silica nanospheres as catalysts for catalytic ozonation systems[50], and the efficient catalytic ozonation by manganese incorporated hierarchical mesoporous silica nanosphere with fibrous morphology[51]. In all of these processes, the use of KCC-1 as a carrier is advantageous in terms of activity and stability. Based on the excellent performance of KCC-1, it can be loaded with metal nanoparticles or organic solvents providing a large number of open holes[37,52]. The magnetic Fe_3O_4 core in the center made the microdrops manipulable, while the open pores on KCC-1 shell provided plenty of space for loading organic phase, and the organic phase on the surface provided the same properties of an organic solvent[52,53]. With ethyl acetate and bisphenol A (BPA) as examples of organic solvents and organic contaminants respectively, the potential for the magnetic organic microdrops to extract organic contaminants from water was discussed detailedly.

Results and discussion

Characterization of superhydrophobic/superoleophilic Fe_3O_4@KCC-1 nanospheres

Figure 2 shows the SEM and TEM images of the *n*-hexyltrimethoxysilane-modified Fe_3O_4@KCC-1 nanospheres. From the SEM images it could be found that the diameter of the nanospheres was about 500 nm to 1 μm. On the surface of the nanospheres there were plenty of pores. The TEM images demonstrated the inner structure of the *n*-hexyltrimethoxysilane-modified Fe_3O_4@KCC-1 nanospheres, from which the core-shell structures could be clearly observed. In the center it was the magnetic core with Fe_3O_4 nanoparticles, and the out layer was KCC-1 shell with pores. Due to the irregular shape of aggregation of magnetic Fe_3O_4 nanoparticles, cracks formed on the surface of the KCC-1 shell of some Fe_3O_4@KCC-1 nanospheres. Moreover, the results from pore analysis showed that the pore volume of

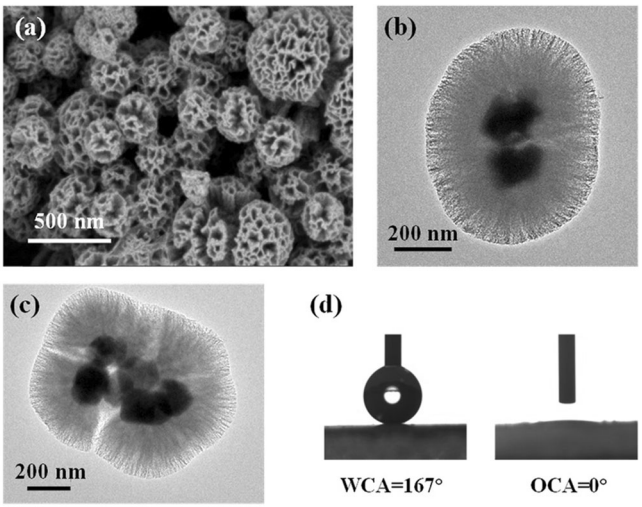

Fig. 2 | The morphology and surface wettability of superhydrophobic/superoleophilic Fe_3O_4@KCC-1 microspheres. a SEM image of superhydrophobic/superoleophilic Fe_3O_4@KCC-1 nanospheres; **b** and **c** TEM images of superhydrophobic/superoleophilic Fe_3O_4@KCC-1 nanospheres; **d** Water (left) and 1,2-dichloroethane (right) contact angles on superhydrophobic/superoleophilic Fe_3O_4@KCC-1 nanospheres.

superhydrophobic/superoleophilic Fe_3O_4@KCC-1 was around 0.68 $cm^3\ g^{-1}$ (see in the Supporting Information).

The surface wettability investigations indicated that water and 1,2-dichloroethane contact angles on the surface of a layer of *n*-hexyltrimethoxysilane-modified Fe_3O_4@KCC-1 nanospheres were 152° and 0°, respectively. It means that the surface was superhydrophobic and superoleophilic, making the nanospheres affiliative for organic solvents and repellant for water.

To further investigate the structure and composition of the superhydrophobic/superoleophilic Fe_3O_4@KCC-1, x-ray photoelectron spectroscopy (XPS), x-ray diffraction (XRD), Fourier transform infrared spectroscopy (FT-IR), thermogravimetric (TG) analysis Table. 1 and magnetism analysis were carried out. Figure 3 shows the XPS spectra of superhydrophobic/superoleophilic Fe_3O_4@KCC-1 nanospheres. From the full-survey spectra (Fig. 3a) the peaks of Si and O could clearly be observed, while the peaks of Fe were very weak although they were distinguishable.

Table 1 | Comparison of BPA removal with different methods

NO.	Method	BPA initial concentration	Base material	Cost and environmental impact.	BPA removal efficiency (%)	Ref.
1	Adsorption method	1 mg/L	Amyloid fibrils aerogel	Efficient and affordable solution biocompatible and environmentally	78	21
2	Adsorption method	50 mg/L	Fe_3O_4@MIL-100(Fe)	Good stability and can be reused	87	62
3	Adsorption method	20 mg/L	Alkali-modified biochar	Low-cost biochar	85.4	63
4	Separation membrane	1 mg/L	Sequential Ultrafiltration-Catalysis Membrane	High efficiency, low energy consumption, easy operation, and low environmental impacts,	95	64
5	Separation membrane	100 mg/L	An in situ-modified membrane by residual hydrolyzed aluminum nanoparticle	Reduce membrane contamination during nanofiltration	88.5	65
6	Separation membrane	1 mg/L	RO membrane	Extended irradiation times and large energy amounts	60–84	66
7	Advanced oxidation process	20 mg/L	$Bi_4O_5Br_2$-MnO_2	Low-cost and high-performance	87	67
8	Advanced oxidation process	15 mg/L	β-SiC/BiOBr	The high chemical stability, temperature resistance, thermal conductivity and mechanical strength	69	68
9	Advanced oxidation process	10 mg/L	$Bi_4O_5Br_2$/α-MnS	The simple construction, physiochemical properties, and reinforced catalytic	78	69
10	Extraction method	50 mg/L	Fe_3O_4@KCC-1@EA	Simple, easy and low cost.	98	This work

The deconvolution of fine spectrum of Fe 2p could result in two spin orbital coupling peaks (Fig. 3b), which was the characteristics of Fe^{3+} and Fe^{2+}. The peaks at 710.4 eV and 723.2 eV corresponded to Fe^{3+}, and the peaks at 712.0 eV and 725.8 eV corresponded to Fe^{2+}[54,55]. In the fine spectrum of Si 2p (Fig. 3c), the peaks at 102.9 eV and 103.6 eV corresponded to the Si-C bonds and Si-O bonds on the modified Fe_3O_4@KCC-1 surface respectively[56]. In the fine spectrum of O 1 s (Fig. 3d) there were two peaks, which corresponded to the O-Si-O bonds (532.4 eV) and the O-Si-C bonds (533.0 eV)[57].

Figure 4a shows the XRD patterns of the superhydrophobic/superoleophilic Fe_3O_4@KCC-1 nanospheres. The peaks at $2\theta = 30.12°$, 35.48°, 37.11°, 43.12°, 53.50°, 57.03°, 62.64°and 74.09° corresponded to the (220), (311), (222), (400), (422), (511), (440) and (533) planes of Fe_3O_4, respectively. These peaks were sharp and strong, indicating that the Fe_3O_4 core had cubic spinel structure. No significant XRD peaks about KCC-1 shell could be distinctly observed as it was lack of crystalline structure.

FT-IR investigation was carried out to further confirm the chemical bonds in superhydrophobic/superoleophilic Fe_3O_4@KCC-1 nanospheres. The results were shown in Fig. 4b. The peak at 570 cm^{-1} corresponded to the vibration of Fe-O bonds in spinel Fe_3O_4 nanoparticles. This peak existed in all the samples. However, the signals in Fe_3O_4@KCC-1 and in superhydrophobic/superoleophilic Fe_3O_4@KCC-1 were weaker. This was caused by the formation of SiO_2 shell on the surface of Fe_3O_4 nanoparticles. The two peaks at 2849 cm^{-1} and 2917 cm^{-1}, weak but significant, might be derived from -CH_2- stretching vibration of the residual surfactants left from Fe_3O_4 nanoparticle preparation. After coating with KCC-1 shell, the peak of bending vibration of Si-O-Si emerged at 467 cm^{-1}, and the peaks of antisymmetric stretching vibration and symmetric stretching vibration of Fe-O-Si emerged at 798 cm^{-1} and 1097 cm^{-1}, respectively. The peak at 3419 cm^{-1} of Fe_3O_4@KCC-1 and superhydrophobic/superoleophilic Fe_3O_4@KCC-1 was attributed to the -OH groups on the surface of KCC-1 shell. This peak became weaker when Fe_3O_4@KCC-1 was turned into superhydrophobic/superoleophilic, because most of the -OH groups reacted with *n*-hexyltrimethoxysilane in this process.

The thermal test results in Fig. 4c showed that there was 94.18% residual weight left for Fe_3O_4@KCC-1, and 91.64% residual weight left for superhydrophobic/superoleophilic Fe_3O_4@KCC-1 after heated to 800 °C. The difference of 2.54% weight loss was attributed to the decomposition of hexyl groups on the surface of superhydrophobic/superoleophilic Fe_3O_4@KCC-1 nanospheres.

The magnetism analyses of the nanospheres were shown in Fig. 4d. Fe_3O_4@KCC-1 nanospheres and superhydrophobic/superoleophilic Fe_3O_4@KCC-1 nanospheres showed superparamagnetism similar to Fe_3O_4 nanoparticles. The magnetization intensities of Fe_3O_4@KCC-1 nanospheres and superhydrophobic/superoleophilic Fe_3O_4@KCC-1 nanospheres were 46.51 emu·g^{-1} and 45.34 emu·g^{-1}, respectively, which were smaller than 80.04 emu·g^{-1} of Fe_3O_4 nanoparticles. The decreasing of magnetization intensity was caused by the coating of nonmagnetic KCC-1 shell on Fe_3O_4 nanoparticles. Nevertheless, it was reported that when the magnetization intensity was higher than 8 emu·g^{-1}, the magnetic separation of nanoparticles could be smoothly realized[58]. The superhydrophobic/superoleophilic Fe_3O_4@KCC-1 nanospheres could be manipulated with an external magnetic field (inset of Fig. 4d).

Removal of organic contaminants from water with Fe_3O_4@KCC-1@EA microdrops

The surface wettability of superhydrophobic/superoleophilic Fe_3O_4@KCC-1 nanospheres made them affinitive for ethyl acetate and repellent for water, therefore ethyl acetate could be easily loaded in the pores on the surface of superhydrophobic/superoleophilic Fe_3O_4@KCC-1 nanospheres and it would not be replaced by water when mixing (Fig. 1). The carrying capacity of superhydrophobic/superoleophilic Fe_3O_4@KCC-1 for ethyl acetate was measured to be 2.67 mL·g^{-1}, which was larger than the pore volume of superhydrophobic/superoleophilic Fe_3O_4@KCC-1 nanospheres, meaning

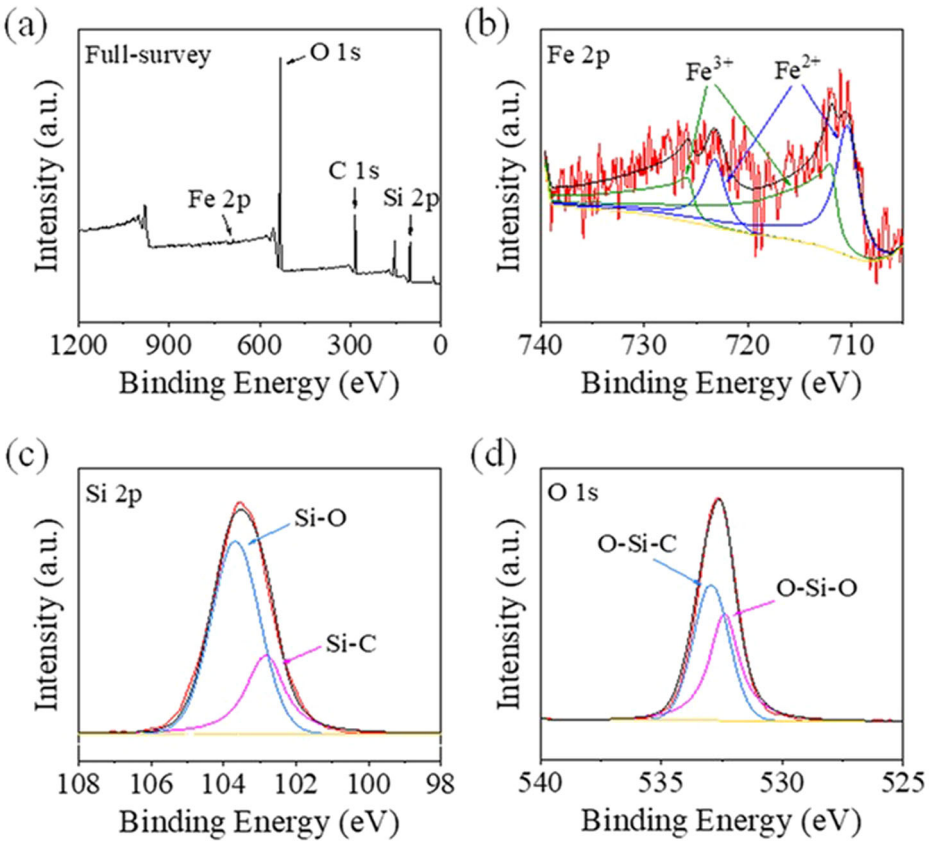

Fig. 3 | The XPS spectra of superhydrophobic/superoleophilic Fe_3O_4@KCC-1 nanospheres. **a** Full-survey XPS spectrum of superhydrophobic/superoleophilic Fe_3O_4@KCC-1 nanospheres. **b** Fe 2P XPS spectra of superhydrophobic/superoleophilic Fe_3O_4@KCC-1 nanospheres. **c** Si 2P XPS spectra of superhydrophobic/superoleophilic Fe_3O_4@KCC-1 nanospheres. **d** O 1S XPS spectra of superhydrophobic/superoleophilic Fe_3O_4@KCC-1 nanospheres.

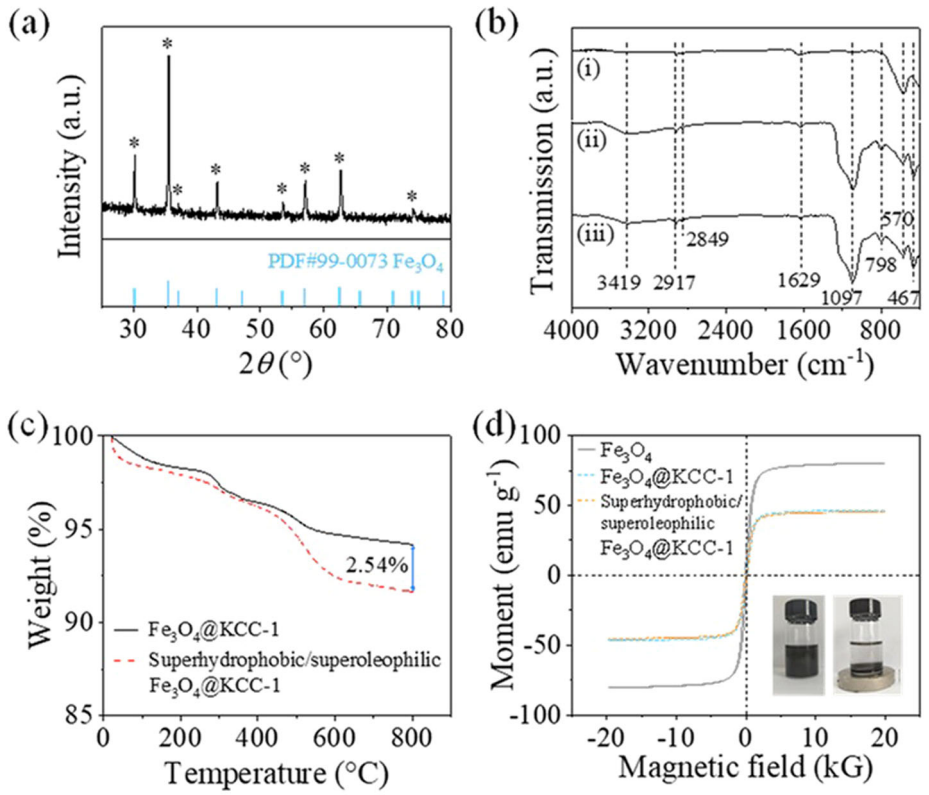

Fig. 4 | Characterization of crystalline structure, chemical composition, and magnetic property of superhydrophobic/superoleophilic Fe_3O_4@KCC-1 microspheres. **a** XRD pattern of superhydrophobic/superoleophilic Fe_3O_4@KCC-1 nanospheres; **b** FT-IR spectra of Fe_3O_4 nanoparticles (i), Fe_3O_4@KCC-1 nanospheres (ii), and superhydrophobic/superoleophilic Fe_3O_4@KCC-1 nanospheres (iii); **c** TG curves of Fe_3O_4@KCC-1 nanospheres (black solid curve) and superhydrophobic/superoleophilic nanospheres (red dashed curve); **d** Vibrating sample magnetometry (VSM) curves of Fe_3O_4 nanoparticles, Fe_3O_4@KCC-1 nanospheres, and superhydrophobic/superoleophilic Fe_3O_4@KCC-1 nanospheres.

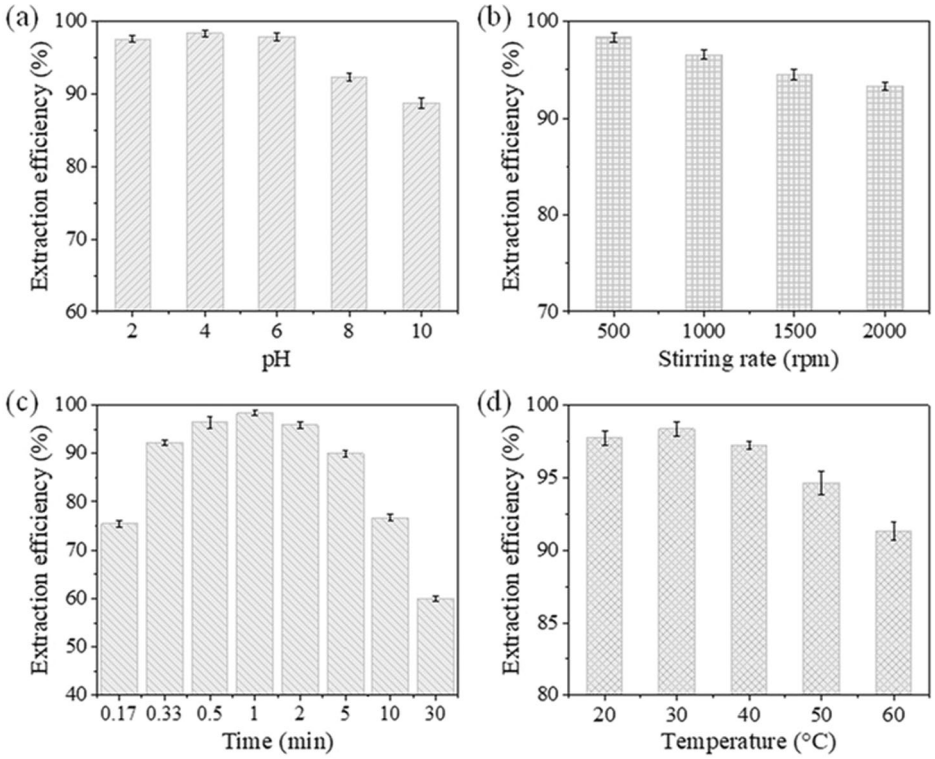

Fig. 5 | The extraction efficiency of BPA with Fe_3O_4@KCC-1@EA microdrops from aqueous solution under different conditions. a pH; **b** stirring rate; **c** stirring time; and **d** temperature.

that there was some ethyl acetate on the surface of KCC-1 shell, not just in the pores (Fig. 1a).

The pH value of an aqueous solution often affects the form of organic contaminants, especially for organic acids and organic bases. BPA is an organic acid which could be ionized in water phase (Equation 1 and 2).

During extraction, there was an equilibrium between the concentrations of BPA in the two phases (Eq. 5).

When the concentration of H_3O^+ increased (pH value decreased), the ionization equilibrium shifted from the right to the left, and the concentration of molecular BPA in water increased (Equation 1 and 2), making the concentration of BPA in ethyl acetate phase increased (Equation 3). The overall result was that more BPA entered Fe_3O_4@KCC-1@EA microdrops. Therefore, lower pH value was beneficial for BPA extraction.

As shown in Fig. 5a, when pH was 8 or higher, the ionization of BPA increased its solubility in water phase, making the extraction efficiency dropped sharply. With the decreasing of pH, the extraction efficiency gradually increased. When pH was 4, the extraction efficiency reached an optimized value of 98.3%. Further decreasing of pH could not induce further increase of extraction efficiency of BPA, as the increasing of molecular BPA became not significant anymore.

Stirring played an important role in accelerating BPA diffusion between the two phases. During the extraction experiments, the mixtures were stirred by a vortex mixer. When stirring rate increased gradually from 500 rpm to 2000 rpm, the extraction efficiency decreased gradually from 98.3% to 93.3%. The faster stirring might accelerate the movement of boundary layer between the two phases and the evaporation of the ethyl acetate, resulting in adverse effect on BPA transferring and reducing the amount of ethyl acetate in the mixtures. These results were consistent with previous literature by Muthuraman et al.[59] and Soniya et al.[60], in which it was reported that lower stirring rate was better for the extraction.

The stirring time was also crucial for optimizing extraction efficiency. The extraction efficiency could be significantly compromised either with too short or too long extraction time. As shown in Fig. 5c, when extraction time increased from 10 s to 1 min, the extraction efficiency gradually increased from 75.5% and reached a maximum of 98.3% at 1 min. Further prolonging extraction time caused gradual decreasing of extraction efficiency, which decreased to 60.0% in 30 min. It means that more and more BPA entered to Fe_3O_4@KCC-1@EA microdrops with time in the 1st min, and the extraction reached equilibrium in 1 min. After that, due to the gradual evaporation of ethyl acetate, BPA started to return to water phase, making the extraction efficiency decreased.

Both extraction equilibrium and the process to reach equilibrium were affected by temperature. To investigate the influence of temperature on BPA extraction with Fe_3O_4@KCC-1@EA from water, the extraction experiments were carried out at different temperature from 20 to 60 °C. As shown in Fig. 5d, the extraction efficiency was 97.7% at 20 °C, while it increased slightly to 98.3% at 30 °C. The increasing of temperature accelerated the substance exchange in the mixture, speeding up the process to reach extraction equilibrium. However, when temperature kept increasing from 30 °C, the extraction efficiency gradually decreased. It reached 91.3% when temperature increased to 60 °C. At higher temperature, ethyl acetate in Fe_3O_4@KCC-1@EA microdrops evaporated faster, making extraction efficiency decreased, although not very much.

The recycling of used materials is an important pathway to reduce cost. After the extraction experiment, the Fe_3O_4@KCC-1@EA microdrops saturated with BPA were collected from water phase with a magnet, washed with ethanol thoroughly, and dried in vacuum at 60 °C for recycling Fe_3O_4@KCC-1 nanospheres. The recycled Fe_3O_4@KCC-1 nanospheres were saturated with ethyl acetated again for another extraction of BPA from water solution. As shown in Fig. 6a, the Fe_3O_4@KCC-1@EA microdrops prepared from the recycled Fe_3O_4@KCC-1 nanospheres showed little decrease in extraction efficiency for BPA after being used for 5 cycles. This was because no significant destruction on the Fe_3O_4@KCC-1 nanospheres was made neither in the preparation of Fe_3O_4@KCC-1@EA microdrops nor in the extraction of BPA. The SEM image of the Fe_3O_4@KCC-1 nanospheres after use displayed in Fig. 6b, from which it could be observed that the morphology of the Fe_3O_4@KCC-1 carrier did not change significantly. The size of the nanospheres was still around 500 nm, and the pore structure on the surface was clearly visible. There was no significant difference compared to the nanospheres before use (Fig. 2a). The unchanged morphology of the Fe_3O_4@KCC-1 carrier ensured excellent recyclability, making the

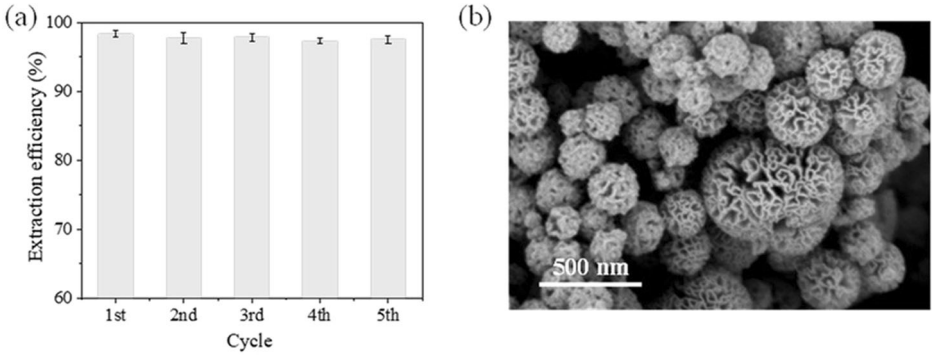

Fig. 6 | The reusability of Fe_3O_4@KCC-1@EA microdrops in in BPA removal from water. a The extraction efficiency of BPA with Fe_3O_4@KCC-1@EA microdrops prepared from recycled Fe_3O_4@KCC-1 nanospheres. **b** SEM image of superhydrophobic/superoleophilic Fe_3O_4@KCC-1 nanospheres after use. The error bars represent the standard deviations of the data.

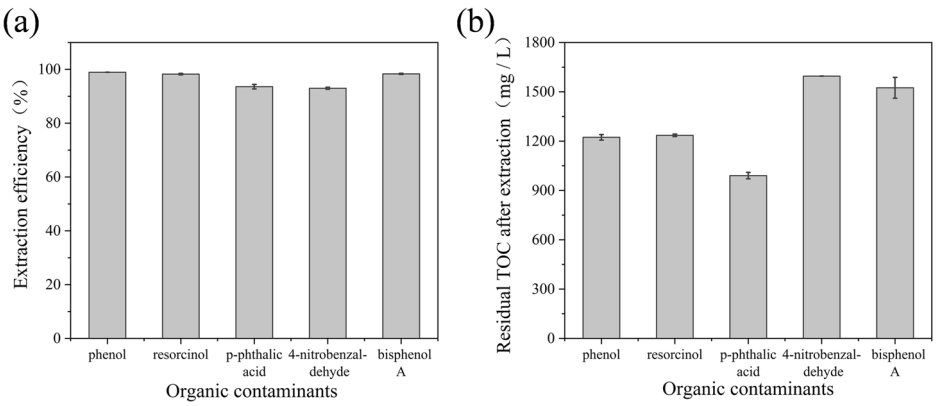

Fig. 7 | The removal of other organic contaminants from water with Fe_3O_4@KCC-1@EA microdrops. a Extraction efficiency of Fe_3O_4@KCC-1@EA microdrops for organic contaminants in different simulated waste water (phenol, resorcinol, *p*-phthalic acid, 4-nitrobenzaldehyde, and bisphenol A); **b** Residual TOC released in aqueous phase after extraction in different simulated waste water. The error bars represent the standard deviations of the data.

Fe_3O_4@KCC-1@EA microdrops very promising for water remediation from organic contaminants.

In addition, the removal efficiencies of Fe_3O_4@KCC-1@EA microdrops for other common organic contaminants were also investigated (phenol, resorcinol, *p*-phthalic acid, and 4-nitrobenzaldehyde), as shown in Fig. 7a. Under the same conditions for BPA removal, the extraction efficiencies were all above 90%, which showed good removal efficiencies. This indicated that Fe_3O_4@KCC-1@EA nanospheres can be widely used to remove other organic contaminants in water. It could provide another way for the purification of organic pollutants in addition to adsorption, advanced oxidation and membrane filtration.

After the removal of organic contaminants, the amount of residual total organic carbon (TOC) in the aqueous solution residual from Fe_3O_4@KCC-1@EA microdrops after extraction was investigated. It could be seen that the residual TOC concentration in the aqueous phase was below 1600 mg/L for all the cases with different organic contaminants. Besides, the residual TOC concentration in the aqueous phase without organic contaminants was 1010 mg/L, meaning that the residual TOC after extraction was mostly caused by the dissolution of ethyl acetate in water. Considering the low environmental harm of ethyl acetate itself, the secondary pollution caused by the extraction process was very little. Nevertheless, it will be better to choose organic solvents with less aqueous solubility for practical purification of water.

In summary, magnetic Fe_3O_4@KCC-1@EA microdrops were fabricated by loading ethyl acetate with superhydrophobic/superoleophilic Fe_3O_4@KCC-1 nanospheres. With BPA as an example, the application of Fe_3O_4@KCC-1@EA microdrops for elimination of organic contaminants from water through extraction has been investigated. The ethyl acetate in the pores on KCC-1 shell provided organic phase to extract and accommodate BPA from water phase. And the magnetic Fe_3O_4 core provided convenience for fast separation of the microdrops saturated with BPA from water phase after the extraction had been completed. Besides BPA elimination with Fe_3O_4@KCC-1@EA microdrops, this method could also be promoted to other organic solvents for other organic contaminants elimination from polluted water. Nevertheless, it should be noted that the present study was on flask-scale. Challenges are faced on the way to practical applications in water remediation for lakes and rivers, for example, the choice of organic solvents, the consumption of organic solvents during extraction, the extraction efficiency for mixed organic contaminants, and the collection of microdrops after extraction from large water body, etc.

Methods

Preparation of Fe_3O_4@KCC-1@EA microdrops

The magnetic carrier of ethyl acetate microdrops was fabricated through a method based on previous reports[52,61]. As shown in Fig. 1a, a layer of SiO_2 was firstly coated on the surface of Fe_3O_4 nanoparticles by the Stöber method, then a KCC-1 shell was prepared on the surface, resulting in Fe_3O_4@KCC-1 nanospheres. The Fe_3O_4@KCC-1 nanospheres were modified with *n*-hexyltrimethoxysilane to make the surface superhydrophobic/superoleophilic. Thereafter ethyl acetate was loaded on the surface to make Fe_3O_4@KCC-1@EA microdrops.

Firstly, 1.0 g Fe_3O_4 nanoparticles (20–30 nm) was dispersed in a mixture of aqueous ammonia (1 mL), anhydrous ethanol (150 mL) and deionized water (30 mL) and made homogeneous under sonication. 2 mL tetraethyl orthosilicate (TEOS) was added under vigorous stirring and the mixed solution was subsequently heated with stirring at 50 °C for 6 h. At the end of the reaction, the solid product was quickly separated using a magnet and washed repeatedly with anhydrous ethanol and deionized water, and the prepared magnetic nanoparticles were recorded as Fe_3O_4/SiO_2 nanospheres.

A liquid mixture (Liquid A) was prepared by dispersing 1.0 g Fe_3O_4/SiO_2 nanospheres in a mixture of cyclohexane (60 mL) and pentanol (3 mL). Another liquid mixture (Liquid B) was prepared by dissolving 2.0 g cetylpyridinium bromide (CPB) and 1.2 g urea in 50 mL deionized water. Liquid A was added to liquid B in sonication, and then 2 mL TEOS was added to the mixture and sonicated at room temperature for 30 min. The reaction solution

was poured into a PTFE-lined autoclave for hydrothermal reaction at 120 °C for 4 h. After the reaction finished, the solid product was quickly separated with a magnet, washed with anhydrous ethanol and deionized water, and dried in vacuum at 60 °C overnight. After drying and grinding finely and wrapped with filter paper, the solid products were extracted in Soxhlet extractor with a mixture of anhydrous ethanol and hydrochloric acid for 48 h. After drying in vacuum at 60 °C, Fe_3O_4@/KCC-1 nanospheres were obtained.

1.0 g Fe_3O_4@KCC-1 nanospheres were dispersed in 5 mL ethanol solution of *n*-hexyltrimethoxysilane (2%), and the mixture was refluxed at 80 °C for 24 h. The solid products were collected with a magnet, washed with ethanol and dried in vacuum to obtain superhydrophobic/superoleophilic Fe_3O_4@KCC-1 nanospheres. Thereafter, ethyl acetate was loaded onto the surface to form Fe_3O_4@KCC-1@EA nanospheres.

Characterization of Fe_3O_4@KCC-1 nanospheres

The morphology and microstructure of the superhydrophobic/superoleophilic Fe_3O_4@KCC-1 were analyzed with scanning electron microscopy (SEM) (Regulus 8100, Hitachi) and transmission electronic microscopy (TEM) (Tecnai G2 F20S, FEI). Prior to SEM tests, the sample was fixed on the stage and was sprayed with gold to improve the conductivity of the surface. In TEM tests, the sample was dispersed evenly in anhydrous ethanol and dropped onto a copper network. TEM tests were carried out after ethanol dried. The composition of the nanospheres was determined by X-ray diffraction (XRD) (Ultima IV, Rigaku), X-ray photoelectron spectroscopy (XPS) (EscaLab 250Xi, ThermoFisher Scientific), Fourier transform-infrared spectroscopy (FT-IR) (Nicolet Is5, ThermoFisher) and thermogravimetric (TG) analysis (STA 449 F5 Jupiter, Netzsch). XRD investigation was carried out on with a scanning rate of 15° min^{-1} and a scanning stride width of 0.06°. XPS investigations were carried out with tube voltage of 40 kV and current of 40 mA. FT-IR spectra were measured using transmission mode with KBr disks. TG analysis was carried out in N_2 atmosphere from room temperature to 800 °C with a heating rate of 10 °C min^{-1}. The static contact angles of water and 1,2-dichloroethane on the nanospheres were analyzed on a contact angle meter (SL250, KINO).

The measurement of carrying capacity of ethyl acetate in Fe_3O_4@KCC-1@EA microdrops

The carrying capacity of Fe_3O_4@KCC-1 nanospheres for ethyl acetate was measured through a method modified from literature by Wang et al.[52] Briefly, 150 mg Fe_3O_4@KCC-1 nanospheres were added into a glass vial with 8 mL water and 1 mL ethyl acetate. After the mixture was vigorously stirred, a magnet was applied under the bottom of vial to collect Fe_3O_4@KCC-1@EA microdrops. And the amount ethyl acetate left on the top was measured. The carrying capacity was calculated according to Eq. 4:

$$\text{carrying capacity} = V_{EA}/m\text{Fe}_3\text{O}_4\text{@KCC} - 1 \quad (4)$$

where V_{EA} was the volume of ethyl acetate absorbed by Fe_3O_4@KCC-1 nanospheres, and $m\text{Fe}_3\text{O}_4\text{@KCC} - 1$ was the mass of Fe_3O_4@KCC-1 nanospheres.

Extraction of BPA and other organic contaminants with Fe_3O_4@KCC-1@EA microdrops

150 mg Fe_3O_4@KCC-1 nanospheres were added into a glass vial, into which 1 mL ethyl acetate and 8 mL water was added thereafter. After the vail was vigorously stirred, the formed Fe_3O_4@KCC-1@EA microdrops were collected and transferred into another glass vial into which 1 mL BPA solution or aqueous solution of other organic contaminants (50 mg L^{-1}, preheated, pH = 4) was added. Immediately after stirring the vials with a vortex mixer at 500 rpm for 1 min (MX-S, DLAB), a magnet was used to separate the Fe_3O_4@KCC-1@EA microdrops from the aqueous phase. The used Fe_3O_4@KCC-1 nanospheres were collected and washed with water and ethanol. And the BPA concentration in the water phase was analyzed with high-performance liquid chromatograph (HPLC, LC5090, FULI) with a UV detector at a wavelength of 278 nm. A welchrom 4.6 mm × 250 mm TC-C18 column was utilized as the stationary phase and the isocratic mobile phase was composed of 60% v/v methanol and 40% v/v Milli-Q water. The sample injection volume was 10 μL, and the flow rate was 1 mL min^{-1}.

With the concentrations of BPA in water phase before and after extraction, the extraction efficiency (*E*) was calculated with Eq. 5:

$$E = \frac{C_{aq,0} - C_{aq,1}}{C_{aq,0}} \times 100\% \quad (5)$$

where $C_{aq,0}$ was the initial BPA concentration in water phase before extraction, which was 50 mg L^{-1} in this study, and $C_{aq,1}$ was the residual BPA concentration in water phase after extraction.

In the cyclic BPA extraction experiments, after each extraction experiment, the magnetic Fe_3O_4@KCC-1@EA microdrops were collected with a magnet, washed with ethanol, and dried in vacuum at 60 °C for next use.

A TOC analyzer (Multi N/C 3100, Analytik Jena) was used to determine the amount of all organic carbon remaining in the aqueous phase after extraction. The samples were studied by the differential subtraction (TC-IC) method, where 300 μL of the sample was taken for each test and injected into the TOC analyzer for determination, the water sample was injected directly into the inorganic carbon reactor to measure the inorganic carbon (IC) and the water sample was injected into the combustion tube to measure the total carbon (TC), and the difference between the TC and the IC was the TOC value.

Data availability

The authors confirm that the data supporting the findings of this study are available within the article and its supplementary materials.

Received: 2 January 2024; Accepted: 29 August 2024;
Published online: 27 September 2024

References

1. Tkaczyk, A., Mitrowska, K. & Posyniak, A. Synthetic organic dyes as contaminants of the aquatic environment and their implications for ecosystems: A review. *Sci. Total Environ.* **717**, 137222 (2020).
2. Glover, C. M., Liu, Y. & Liu, J. X. Assessing the risk from trace organic contaminants released via greywater irrigation to the aquatic environment. *Water Res.* **205**, 117664 (2021).
3. Ahmed, M. et al. Recent developments in hazardous pollutants removal from wastewater and water reuse within a circular economy. *Npj Clean. Water* **5**, 12 (2022).
4. Praveen, S., Jegan, J., Pushpa, T. B., Gokulan, R. & Bulgariu, L. Biochar for removal of dyes in contaminated water: an overview. *Biochar* **4**, 10 (2022).
5. Ren, Y. F., Yu, F., Li, X. G. & Ma, J. Recent progress on adsorption and membrane separation for organic contaminants on multi-dimensional graphene. *Mater. Today Chem.* **22**, 100603 (2021).
6. Yap, P. L. et al. Graphene-Based Sorbents for Multipollutants Removal in Water: A Review of Recent Progress. *Adv. Funct. Mater.* **31**, 2007356 (2021).
7. Song, Y. Y. et al. Heterostructure particles enable omnidispersible in water and oil towards organic dye recycle. *Nat. Commun.* **14**, 5779 (2023).
8. Alsawy, T., Rashad, E., El-Qelish, M. & Mohammed, R. H. A comprehensive review on the chemical regeneration of biochar adsorbent for sustainable wastewater treatment. *Npj Clean. Water* **5**, 29 (2022).
9. Luo, X. F., Zhu, Z. P., Tian, Y., You, J. & Jiang, L. Titanium Dioxide Derived Materials with Superwettability. *Catalysts* **11**, 425 (2021).
10. Liu, K. S., Cao, M. Y., Fujishima, A. & Jiang, L. Bio-Inspired Titanium Dioxide Materials with Special Wettability and Their Applications. *Chem. Rev.* **114**, 10044–10094 (2014).

11. Tufail, A., Price, W. E., Mohseni, M., Pramanik, B. K. & Hai, F. S. I. A critical review of advanced oxidation processes for emerging trace organic contaminant degradation: Mechanisms, factors, degradation products, and effluent toxicity. *J. Water Process Eng.* **40**, 101778 (2021).
12. Coha, M., Farinelli, G., Tiraferri, A., Minella, M. & Vione, D. Advanced oxidation processes in the removal of organic substances from produced water: Potential, configurations, and research needs. *Chem. Eng. J.* **414**, 128668 (2021).
13. Guo, K. H., Wu, Z. H., Chen, C. Y. & Fang, J. Y. UV/Chlorine Process: An Efficient Advanced Oxidation Process with Multiple Radicals and Functions in Water Treatment. *Acc. Chem. Res.* **55**, 286–297 (2022).
14. Abd El-Monaem, E. M. et al. A comprehensive review on LDH-based catalysts to activate persulfates for the degradation of organic pollutants. *Npj Clean. Water* **6**, 34 (2023).
15. Zhang, J. et al. Two dimensional nanomaterial-based separation membranes. *Electrophoresis* **40**, 2029–2040 (2019).
16. George, J. et al. Biocatalytic polymeric membranes to decrease biofilm fouling and remove organic contaminants in wastewater: a review. *Environ. Chem. Lett.* **20**, 1897–1927 (2022).
17. Li, C. et al. Ultrastable Co-NC membrane for sterilization of Escherichia coli in flowing water. *Npj Clean. Water* **6**, 47 (2023).
18. Li, X. et al. Water Contaminant Elimination Based on Metal-Organic Frameworks and Perspective on Their Industrial Applications. *Acs Sustain Chem. Eng.* **7**, 4548–4563 (2019).
19. Rojas, S. & Horcajada, P. Metal-Organic Frameworks for the Removal of Emerging Organic Contaminants in Water. *Chem. Rev.* **120**, 8378–8415 (2020).
20. Song, Y. P., Phipps, J., Zhu, C. J. & Ma, S. Q. Porous Materials for Water Purification. *Angew. Chem. Int Ed.* **62**, e202216724 (2023).
21. Mon, M. et al. Multivariate Metal-Organic Frameworks for the Simultaneous Capture of Organic and Inorganic Contaminants from Water. *J. Am. Chem. Soc.* **141**, 13601–13609 (2019).
22. Ji, X. F. et al. Removal of Organic Micropollutants from Water by Macrocycle-Containing Covalent Polymer Networks. *Angew. Chem. Int Ed.* **59**, 23402–23412 (2020).
23. Yang, J. J., Shojaei, S. & Shojaei, S. Removal of drug and dye from aqueous solutions by graphene oxide: Adsorption studies and chemometrics methods. *Npj Clean. Water* **5**, 5 (2022).
24. Peydayesh, M. et al. Amyloid Fibrils Aerogel for Sustainable Removal of Organic Contaminants from Water. *Adv. Mater.* **32**, 1907932 (2020).
25. Ravindiran, G. et al. Removal of azo dyes from synthetic wastewater using biochar derived from sewage sludge to prevent groundwater contamination. *Urban Clim.* **49**, 101502 (2023).
26. Wang, Y. et al. Efficient removal of phytochrome using rice straw-derived biochar: Adsorption performance, mechanisms, and practical applications. *Bioresour. Technol.* **376**, 128918 (2023).
27. Azhar, M. R. et al. Adsorptive removal of antibiotic sulfonamide by UiO-66 and ZIF-67 for wastewater treatment. *J. Colloid Inter. Sci.* **500**, 88–95 (2017).
28. Chen, X. X. et al. Enhanced H2O2 utilization efficiency in Fenton-like system for degradation of emerging contaminants: Oxygen vacancy-mediated activation of O2. *Water Res* **230**, 119562 (2023).
29. Shan, H. R. et al. Highly flexible, mesoporous structured, and metallic Cu-doped C/SiO2 nanofibrous membranes for efficient catalytic oxidative elimination of antibiotic pollutants. *Nanoscale* **11**, 14844–14856 (2019).
30. Brillas, E. & Peralta-Hernandez, J. M. Removal of paracetamol (acetaminophen) by photocatalysis and photoelectrocatalysis. A critical review. *Sep. Purif. Technol.* **309**, 122982 (2023).
31. Fan, W. et al. Enhanced Photocatalytic Water Decontamination by Micro-Nano Bubbles: Measurements and Mechanisms. *Environ. Sci. Technol.* **55**, 7025–7033 (2021).
32. Tian, S. Q. et al. Heterogeneous catalytic ozonation of atrazine with Mn-loaded and Fe-loaded biochar. *Water Res* **193**, 116860 (2021).
33. Lashuk, B. & Yargeau, V. A review of ecotoxicity reduction in contaminated waters by heterogeneous photocatalytic ozonation. *Sci. Total Environ.* **787**, 147645 (2021).
34. Chen, X. W., Gudda, F. O., Hu, X. J., Waigi, M. G. & Gao, Y. Z. Degradation of bisphenol A in an oxidation system constructed from Mo2C MXene and peroxymonosulfate. *Npj Clean. Water* **5**, 66 (2022).
35. Dong, X., Chen, Z., Tang, A., Dionysiou, D. D. & Yang, H. Mineral modulated single atom catalyst for effective water treatment. *Adv. Funct. Mater.* **32**, 2111565 (2022).
36. Ntelane, T. S., Feleni, U., Mthombeni, N. H. & Kuvarega, A. T. Sulfate radical-based advanced oxidation process (SR-AOP) on titania supported mesoporous dendritic silica (TiO2/MDS) for the degradation of carbamazepine and other water pollutants. *Colloids Surf. a-Physicochemical Eng. Asp.* **655**, 103849 (2022).
37. Afzal, S., Pan, K., Duan, D., Wei, Y. & Chen, L. Heterogeneous activation of peroxymonosulfate with cobalt incorporated fibrous silica nanospheres for the degradation of organic pollutants in water. *Appl. Surf. Sci.* **542**, 148674 (2021).
38. Bentel, M. J., Mason, M. M. & Cates, E. L. Synthesis of Petitjeanite Bi3O(OH)(PO4)2 Photocatalytic Microparticles: Effect of Synthetic Conditions on the Crystal Structure and Activity toward Degradation of Aqueous Perfluorooctanoic Acid (PFOA). *ACS Appl. Mater. Interfaces* **15**, 20854–20864 (2023).
39. Zhang, Y. M. et al. Continuous air purification by aqueous interface filtration and absorption. *Nature* **610**, 74–80 (2022).
40. Wang, Y. et al. Infused-liquid-switchable porous nanofibrous membranes for multiphase liquid separation. *Nat. Commun.* **8**, 575 (2017).
41. Nasrollahi, N., Vatanpour, V. & Khataee, A. Removal of antibiotics from wastewaters by membrane technology: Limitations, successes, and future improvements. *Sci. Total Environ.* **838**, 156010 (2022).
42. Kim, S. et al. Removal of contaminants of emerging concern by membranes in water and wastewater: A review. *Chem. Eng. J.* **335**, 896–914 (2018).
43. Han, Y., Xu, Z. & Gao, C. Ultrathin Graphene Nanofiltration Membrane for Water Purification. *Adv. Funct. Mater.* **23**, 3693–3700 (2013).
44. Jafarian, H. et al. Synthesis of heterogeneous metal organic Framework-Graphene oxide nanocomposite membranes for water treatment. *Chem. Eng. J.* **455**, 140851 (2023).
45. Kuang, B. A., Xiang, X. M., Su, P. C., Yang, W. L. & Li, W. B. Self-assembly of stable and high-performance molecular cage-crosslinked graphene oxide membranes for contaminant removal. *J. Hazard Mater.* **439**, 129708 (2022).
46. Polshettiwar, V., Cha, D., Zhang, X. & Basset, J. M. High-Surface-Area Silica Nanospheres (KCC-1) with a Fibrous Morphology. *Angew. Chem.-Int. Ed.* **49**, 9652–9656 (2010).
47. Lyu, L., Zhang, L., Hu, C. & Yang, M. Enhanced Fenton-catalytic efficiency by highly accessible active sites on dandelion-like copper–aluminum–silica nanospheres for water purification. *J. Mater. Chem. A* **4**, 8610–8619 (2016).
48. Naghizadeh, A., Etemadinia, T., Derakhshani, E. & Esmati, M. Graphitic carbon nitride loaded on powdered mesoporous silica nanoparticles for photocatalytic tetracycline antibiotic degradation under UV-C light irradiation. *Res. Chem. Intermed.* **49**, 1165–1177 (2023).
49. Esmati, M., Allahresani, A. & Naghizadeh, A. Synthesis and characterization of Graphitic Carbon Nitride/Mesoporous Nano-Silica (g-C3N4/KCC-1) nanocomposite as a novel highly efficient and recyclable photocatalyst for degradation of antibiotic in aqueous solution. *Res. Chem. Intermed.* **47**, 1447–1469 (2021).
50. Bai, Z., Wang, J. & Yang, Q. Iron doped fibrous-structured silica nanospheres as efficient catalyst for catalytic ozonation of sulfamethazine. *Environ. Sci. Pollut. Res.* **25**, 10090–10101 (2018).
51. Afzal, S., Quan, X., Chen, S., Wang, J. & Muhammad, D. Synthesis of manganese incorporated hierarchical mesoporous silica nanosphere with fibrous morphology by facile one-pot approach for efficient catalytic ozonation. *J. Hazard. Mater.* **318**, 308–318 (2016).

52. Wang, B. et al. Superhydrophobic magnetic core-shell mesoporous organosilica nanoparticles with dendritic architecture for oil-water separation. *Mater. Chem. Front.* **4**, 2184–2191 (2020).
53. Sarcletti, M. et al. Superoleophilic magnetic iron oxide nanoparticles for effective hydrocarbon removal from water. *Adv. Funct. Mater.* **29**, 1805742 (2019).
54. Wan, Z. & Wang, J. L. Degradation of sulfamethazine using Fe3O4-Mn3O4/reduced graphene oxide hybrid as Fenton-like catalyst. *J. Hazard Mater.* **324**, 653–664 (2017).
55. Wilson, D. & Langell, M. A. XPS analysis of oleylamine/oleic acid capped Fe3O4 nanoparticles as a function of temperature. *Appl. Surf. Sci.* **303**, 6–13 (2014).
56. Sun, L., Han, C., Wu, N., Wang, B. & Wang, Y. D. High temperature gas sensing performances of silicon carbide nanosheets with an n-p conductivity transition. *Rsc Adv.* **8**, 13697–13707 (2018).
57. Chandrasekar, M. S. & Srinivasan, N. R. Role of SiOx on the photoluminescence properties of beta-SiC. *Ceram. Int* **42**, 8900–8908 (2016).
58. Kumar, A., Khan, M., Zeng, X. K. & Lo, I. M. C. Development of g-C3N4/TiO2/Fe3O4@SiO2 heterojunction via sol-gel route: A magnetically recyclable direct contact Z-scheme nanophotocatalyst for enhanced photocatalytic removal of ibuprofen from real sewage effluent under visible light. *Chem. Eng. J.* **353**, 645–656 (2018).
59. Muthuraman, G. & Ibrahim, M. M. Removal of anionic dye from aqueous solution using a cationic carrier. *Int. J. Ind. Chem.* **4**, 15 (2013).
60. Soniya, M. & Muthuraman, G. Comparative study between liquid-liquid extraction and bulk liquid membrane for the removal and recovery of methylene blue from wastewater. *J. Ind. Eng. Chem.* **30**, 266–273 (2015).
61. Li, R. et al. Magnetic dendritic KCC-1 nanosphere-supported cobalt composite as a separable catalyst for hydrogen generation from NaBH4 hydrolysis. *Int. J. Hydrog. Energy* **48**, 25315–25327 (2023).
62. Liu, Q. et al. An efficient method to enrich, detect and remove bisphenol A based on Fe_3O_4@MIL-100(Fe). *Microchemical J.* **165**, 106168 (2021).
63. Tang, Y. et al. Removal of emerging contaminants (bisphenol A and antibiotics) from kitchen wastewater by alkali-modified biochar. *Sci. Total Environ.* **805**, 150158 (2022).
64. Xie, J. et al. Sequential Ultrafiltration-Catalysis Membrane for Excellent Removal of Multiple Pollutants in Water. *Environ. Sci. Technol.* **55**, 2652–2661 (2021).
65. Wang, P. et al. Strong improvement of nanofiltration performance on micropollutant removal and reduction of membrane fouling by hydrolyzed-aluminum nanoparticles. *Water Res.* **175**, 115649 (2020).
66. Fonseca, F. V. et al. Treatment of Bisphenol A (BPA) in water using UV/H2O2 and reverse osmosis (RO) membranes: assessment of estrogenic activity and membrane adsorption. *Water Sci. Technol.* **80**, 2169–2178 (2019).
67. Wang, J. et al. Synergistic effect of well-defined dual sites boosting the oxygen reduction reaction. *Energy Environ. Sci.* **11**, 3375–3379 (2018).
68. Zhang, L., Hao, J., Jia, Z. & Wang, C. Visible light responding β-SiC/BiOBr S-scheme heterojunction photocatalyst with improved photodegradation efficiency of bisphenol A. *J. Solid State Chem.* **325**, 124167 (2023).
69. Huang, X. et al. Separation of perfluorinated electron specialty gases on microporous carbon adsorbents with record selectivity. *Sep. Purif. Technol.* **292**, 121059 (2022).

Acknowledgements

This work was financially supported by Natural Science Foundation of Sichuan Province (No. 2022NSFSC0282).

Author contributions

Jia Lyu: methodology, investigation, formal analysis, writing-original draft preparation. Fengming Zhang: methodology, investigation, formal analysis. Ran Li: methodology, investigation, formal analysis. Jinlin Song: formal analysis, writing-original draft preparation. Qing Liu: investigation, formal analysis. Jinyu Liu: investigation, formal analysis. Hua Dong (corresponding author): conceptualization, funding acquisition, resources, supervision, writing-review and editing.

Competing interests

The authors declare no competing interests.

Additional information

Supplementary information The online version contains supplementary material available at https://doi.org/10.1038/s41545-024-00379-6.

Correspondence and requests for materials should be addressed to Hua Dong.